Applied Energy 371 (2024) 123669

Contents lists available at ScienceDirect

Applied Energy

journal homepage: www.elsevier.com/locate/apenergy

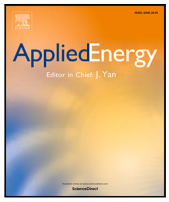

A novel control strategy to neutralize internal heat source within solid oxide electrolysis cell (SOEC) under variable solar power conditions

Zhaojian Liang [a], Shanlin Chen [a], Meng Ni [b], Jingyi Wang [c,1], Mengying Li [a,*,1]

[a] Department of Mechanical Engineering & Research Institute for Smart Energy, The Hong Kong Polytechnic University, Hong Kong Special Administrative Region
[b] Department of Building and Real Estate, Hong Kong Polytechnic University, Hung Hom, Kowloon, Hong Kong, China
[c] School of Science, Harbin Institute of Technology, Shenzhen, 518055, China

ARTICLE INFO

Keywords:
Green hydrogen production
Solid oxide cell
Transient simulation
Dynamic response
Thermal management
Control strategy

ABSTRACT

The integration of solid oxide electrolysis cells (SOECs) with a photovoltaic (PV) system presents a viable method of storing variable solar energy through the production of green hydrogen. To ensure the safety and longevity of SOEC amidst dramatic fluctuations in solar power, control strategies are needed to limit temperature gradients and rates of temperature change within the cell. Recognizing that the supply of the reactant influences the current, a novel control strategy is developed to modulate internal heat source in the SOEC by adjusting the steam flow rate. The effectiveness of this strategy is assessed through numerical simulations conducted on a coupled PV-SOEC system using actual solar irradiance data. The irradiance data are recorded at two-second intervals to account for rapid changes in solar exposure. The results indicate that conventional control strategies, which increase airflow rates, are inadequate in effectively suppressing the rate of temperature variation in scenarios of drastic changes in solar power. In contrast, our proposed strategy demonstrates precise management of SOEC internal heat generation, thus reducing the temperature gradient and variation within the cell to less than 5 K cm^{-1} and 1 K min^{-1}, respectively, and maintaining a high electricity-to-hydrogen conversion efficiency of 94.9%.

1. Introduction

Renewable energy sources, especially solar and wind, are increasing their significance in the energy structure of today [1]. Renewable energy is expected to account for 80% of the new power capacity by 2030, with solar PV alone contributing more than 50% [2]. However, the grid integration of solar and wind power still faces challenges. For instance, the intermittence and variability of power generation can introduce great difficulties in the system operation and management (e.g., a mismatch between generation and load). The uncertainty in power generation necessitates a time-spanning storage system, where green hydrogen emerges as a potential solution to these challenges, serving as a promising seasonal energy storage medium. Due to its long-term chemical stability, transportability, and carbon-free energy conversion [3], hydrogen is increasingly viewed as a viable option for the storage of renewable energy. Consequently, power-to-hydrogen systems have received significant attention in recent years [4].

The SOEC is a promising high-temperature electrolysis device for hydrogen production, because of its high efficiency and operational flexibility. Notably, the SOEC can switch to a solid oxide fuel cell (SOFC) mode for power generation and can accommodate various types of fuels [5,6]. The integration of a PV system with SOEC offers an effective approach to store solar energy in the form of chemical energy contained in hydrogen. PV panels harness solar energy to generate electrical power, which is subsequently utilized by the SOEC for water splitting and hydrogen production. However, the intermittent nature of solar power is a challenge to the thermal management of SOEC. During SOEC operation, temperature gradients can induce thermal stress [7], potentially leading to delamination and cracks in the electrolyte and electrodes [8]. Furthermore, the rapid rate of variation in temperature can result in thermal fatigue [9] and undermine the durability of SOEC.

Numerous studies have investigated the dynamic thermal management of SOEC and SOFC in various scenarios, such as operations under fluctuating wind [9,10] and solar power [11], the switch between fuel cell and electrolyzer [12,13], and load changes [14–16]. Several parameters have been found to be effective for temperature control of SOEC and SOFC, including air flow rate [13–15,17–19], steam/fuel flow rate [19–21], inlet temperature [22,23], and inlet gas compositions [8,24–26]. For example, Wang et al. [9] modulated

* Corresponding author.
E-mail addresses: wangjingyi@hit.edu.cn (J. Wang), mengying.li@polyu.edu.hk (M. Li).
[1] The two authors have the same contribution to this study.

https://doi.org/10.1016/j.apenergy.2024.123669
Received 6 February 2024; Received in revised form 4 May 2024; Accepted 7 June 2024
Available online 24 June 2024

Nomenclature

Symbols

ΔG	Gibbs free energy change of water formation, [J mol^{-1}]
ΔT	Temperature difference, [K]
Δt	Time step size, [s]
δ	Thickness, [m]
$\Delta \mathcal{H}_f$	Enthalpy of formation of water, [J mol^{-1}]
ΔS_f	Entropy of formation of water, [J mol^{-1} K^{-1}]
$\dot{\mathcal{H}}$	Enthalpy flux, [W]
$\dot{\mathcal{V}}$	Volumetric flow rate, [m^3 s^{-1}]
$\dot{m}$	Mass flow rate, [kg s^{-1}]
$\dot{Q}_{H2}$	Hydrogen production rate, [L h^{-1}]
η	Overpotential, [V]
$\mathcal{H}$	Enthalpy, [J]
$\mathcal{R}$	Ideal gas constant, [J mol^{-1} K^{-1}]
μ	Short-circuit current temperature coefficient, [A K^{-1}]
ϕ	Electrical potential, [V]
ρ	Density, [kg m^{-3}]
τ_h	Heat-transfer time constant, [s]
A_{act}	Active area, [m^{-2}]
A_{ch}	Cross area of fluid channel, [m^{-2}]
c_p	Specific heat, [J kg^{-1} K^{-1}]
E_g	Silicon-based PV panel band-gap, [eV]
F	Faraday constant, [C mol^{-1}]
G	Global horizontal irradiance, [W m^{-2}]
I	Current, [A]
i	Current density, [A m^{-2}]
k_B	Boltzmann constant, [J K^{-1}]
L	Length, [m]
m	Mass, [kg]
M_i	Molar mass of species i, [kg mol^{-1}]
n	Number of participating electrons for hydrogen production
n_p	Number of devices connected in parallel
n_s	Number of devices connected in series
P	Power, [W]
p	Pressure, [Pa]
q	Elementary charge, [C]
R	Electrical resistance, [Ω]
S_H	Heat source, [W]
S_{Ohm}	Ohmic heat source, [W]
S_{op}	Overpotential heat source, [W]
S_{rev}	Reversible heat source, [W]
T	Temperature, [K]
t	Time, [s]
U	Voltage, [V]
V	Velocity, [m s^{-1}]
W	Width, [m]
X_i	Mole fraction of species i

Subscripts

act	Active
ave	Average
ch	Channel
E	Electrolyte
ele	Electronic
int	Interconnect
lim	Limit
p	Parallel
s	Series
SCh	Single-channel model
TN	Thermal neutrality

Superscripts

eff	Effective
FL	Functional layer
theo	Theoretical

Abbreviations

ADL	Anode diffusion layer
AFL	Anode functional layer
BC	Boundary condition
CDL	Cathode diffusion layer
CFL	Cathode functional layer
GHI	Global horizontal irradiance
MPP	Maximum power point
PV	Photovoltaic
SOEC	Solid oxide electrolysis cell
SOFC	Solid oxide fuel cell
UDF	User Defined Function

the air flow rate in response to wind power, successfully limiting the temperature gradient within the SOEC. However, they discovered that a significantly high air flow rate is necessary to maintain the temperature variation rate below the targeted 1 K min^{-1} under highly fluctuating power conditions. Such a high air flow rate would require substantial compressor work. Sun et al. [24] suggested that a control method that focuses on the heat source is the key to constrain temperature fluctuations within SOECs. Therefore, they integrated thermochemical energy storage systems with SOEC to balance variations in the heat source. However, the temperature fluctuations in SOEC remain significant under severe power variations. Although existing studies have shown some success in temperature control, effective thermal management remains a challenge for SOEC under highly fluctuating renewable power.

Given the aforementioned challenges, the concept of thermal neutrality could be a potential solution to the thermal management issues. Theoretically, SOEC can operate at thermoneutral voltage (TNV), which reduces the total internal heat source to zero, leading to a more uniform temperature field (although not perfectly uniform). In TNV, the endothermic effect of water-splitting reactions counterbalances Joule heating and overpotential heat generation [9], thus simplifying thermal management [27,28]. In practice, TNV is not a constant value but varies with operating conditions [9]. This fact implies that adjusting operating conditions can neutralize the internal heat source in SOEC, potentially maintaining the SOEC near the thermoneutral state even under fluctuating power supplies. This approach could significantly improve the thermal uniformity and stability of SOECs. However, existing research lacks a detailed exploration of operating strategies designed to regulate the internal heat source in SOECs, leading to a notable research gap. In this context, "internal heat source" refers to the net heat produced or consumed within the SOEC due to electrochemical reactions and overpotentials.

To fill the research gap, we introduce a novel strategy for controlling the internal heat source in SOEC under fluctuating solar power. This is

achieved by modulating the steam supply rate according to real-time solar irradiance level. The control of internal heat source represents a novel direction in SOEC thermal management research, diverging from previous studies that primarily focused on mitigating temperature fluctuations through external interventions, such as increasing airflow. The effectiveness of the proposed control strategy is evaluated using a three-dimensional transient numerical model of SOEC. Besides, we notice that the renewable power data utilized in previous studies are often recorded with low temporal resolution, such as 5 min [26] or 15 min [9,12]. The large time interval in solar data, however, overlooks the highly dynamic nature of renewable power sources. For instance, the solar irradiance can drop from 1000 W m^{-2} to 300 W m^{-2} within several seconds due to cloud attenuation. Thus, using solar data with low temporal resolutions could fail to capture these abrupt changes in irradiance, thereby potentially skewing the evaluation of PV-SOEC performance. To address this gap, we captured solar irradiance data at a significantly smaller time interval — every 2 s. This high-resolution data was then used to assess the effectiveness of our proposed control strategy.

In the following, Section 2 introduces the methodologies employed in this study, including data acquisition and numerical models; Section 3 provides comprehensive derivation and discussion of the proposed control strategy. Overall conclusion follows in Section 4.

2. Methods

As shown in Fig. 1a, this study aims to control the temperature of SOEC under fluctuating solar power supply. To numerically evaluate the effectiveness of our control strategy, we simulate an integrated PV-SOEC system as a case study. The PV panels convert the solar irradiance into electrical power, which is subsequently used in SOEC to split water to produce hydrogen. Note that here we assume the PV panels to be placed horizontally, so they will utilize global horizontal irradiance (GHI) instead of plane-or-array irradiance. In our numerical model, the measured solar irradiance is converted into solar power data through a PV model. The solar power is then applied in our SOEC model for numerical simulation. The proposed control strategy is to dynamically adjust the SOEC steam flow rate in response to solar power, ensuring the thermal safety of the SOEC.

2.1. Solar irradiance measurement

The GHI is measured using a pyranometer with a field of view of 180° (CMP10 produced by Kipp&Zonen, ISO 9060 spectrally flat Class A), installed on the rooftop located on the campus of The Hong Kong Polytechnic University (22.3046°N, 114.1796°E). The GHI data is collected every 2 s to generate a high-temporal-resolution dataset. In addition, to capture the cloud field of the sky, sky images are captured every minute using a 180° fisheye camera (FE9380-HV produced by VIVOTEK Corporation).

2.2. PV model

The PV model utilized in our study is adapted from Refs. [29,33]. As depicted in Fig. 1a, the PV system under investigation comprises two monocrystalline PV panels, each with a nominal power rating of 270 W. The number of PV panels is designed based on the operating range of the SOEC stack, which will be detailed in Section 2.4. An equivalent diode circuit model [29], shown in Fig. 1c, is utilized to calculate the operating current and voltage of a PV panel. This model operates under the assumption that the series internal resistance R_s is nearly zero and the shunt resistance R_{sh} approaches infinity. The mathematical model for the two-panel system can be expressed as

$$I_{PV} = n_p^{PV}\left\{ I_{ph} - I_0\left[\exp\left(\frac{qU_{PV}}{mk_B T_{PV} n_s^{PV}}\right) - 1\right]\right\}, \tag{1}$$

where, $n_p^{PV} = 2$ represents the number of PV panels connected in parallel, $n_s^{PV} = 60$ denotes the number of solar cells connected in series within a single PV panel. $q = 1.60 \times 10^{-19}$ C is the elementary charge. $m = 1$ is the ideal factor of the diode. $k_B = 1.38 \times 10^{-23}$ J K^{-1} is the Boltzmann constant. The photo-generated current I_{ph} is calculated as

$$I_{ph} = \frac{G}{G_{PV,ref}}\left[I_{ph,ref} + \mu\left(T_{PV} - T_{PV,ref}\right)\right], \tag{2}$$

where, $G_{PV,ref} = 1000$ W m^{-2} is the reference solar radiation. $T_{PV,ref} = 298$ K is the reference temperature. $I_{ph,ref} = 9.43$ A is the photo-generated current under the reference solar irradiance. $\mu = 0.00047$ A K^{-1} is the short-circuit current temperature coefficient. The diode reverse saturation current I_0 is calculated as

$$I_0 = I_{0,ref}\left(\frac{T_{PV}}{T_{PV,ref}}\right)^3 \exp\left[\frac{qE_g}{k_B}\left(\frac{1}{T_{PV,ref}} - \frac{1}{T_{PV}}\right)\right], \tag{3}$$

where, $I_{0,ref} = 1.25 \times 10^{-9}$ A is the diode reverse saturation current in the reference state. The band gap E_g of the PV cell is calculated as [29]

$$E_g = 1.17 - \frac{4.73 \times 10^{-4} T_{PV}^2}{T_{PV} + 636}. \tag{4}$$

Combining Eqs. (1)–(4), it is convenient to acquire the current–voltage curve of the PV system given a solar irradiance value G, as shown in Fig. 1e. The maximum power point (MPP) tracker can be used to operate the PV system at its MPP. When n_p^{PV}, n_s^{PV} and T_{PV} of the PV system are held constant at 25 °C, the maximum power P_{PV}^{MPP} can be determined from Fig. 1e and the following equation

$$P_{PV}^{MPP} = I_{PV}^{MPP} U_{PV}^{MPP}. \tag{5}$$

The relationship between the maximum power P_{PV}^{MPP} and solar irradiance G can be extracted from Fig. 1e, which is then regressed as follows to implement into our numerical model,

$$P_{PV}^{MPP} = 3.4737 \times 10^{-5} \cdot G^2 + 0.5106 \cdot G - 3.4792. \tag{6}$$

2.3. SOEC single-channel model

Fig. 1d shows the geometry and working principle of SOEC. The electron conductors within SOEC include interconnects, Anode Diffusion Layer (ADL), Anode Functional Layer (AFL), Cathode Functional Layer (CFL), and Cathode Diffusion Layer (CDL). The ADL, AFL, CDL, and CFL are porous mediums for gas transport. At high temperatures, oxygen ions can travel within the AFL, CFL, and solid oxide electrolyte. In functional layers where electrons, ions, and gases gather, H_2O is split into hydrogen and oxygen through electrochemical reactions.

To simulate the performance of the SOEC stack, we have developed a 3-D single-channel Computational Fluid Dynamics (CFD) model, ensuring a balance between computational cost and accuracy [34,35]. The 3D CFD model, shown in Fig. 1d, is an established model developed and validated in our previous work [31]. This model was built using Ansys Fluent R18.1, a commercial CFD software.

The model solves a coupled set of conservation equations for momentum, mass of species, energy, electronic charge, and ionic charge. These solutions yield transient results for velocity, mass fractions of species, temperature, and electrical and ionic potentials within SOEC. Our model [31] incorporates the following theoretical principles:

- Fick's Law is employed to model gas diffusion within fluid channels. This process accounts for variations in temperature and pressure. In porous media, Extended Fick's law is used to consider the influence of microstructure on gas diffusivity.
- Electrochemical reactions are modeled using the Butler–Volmer equation.

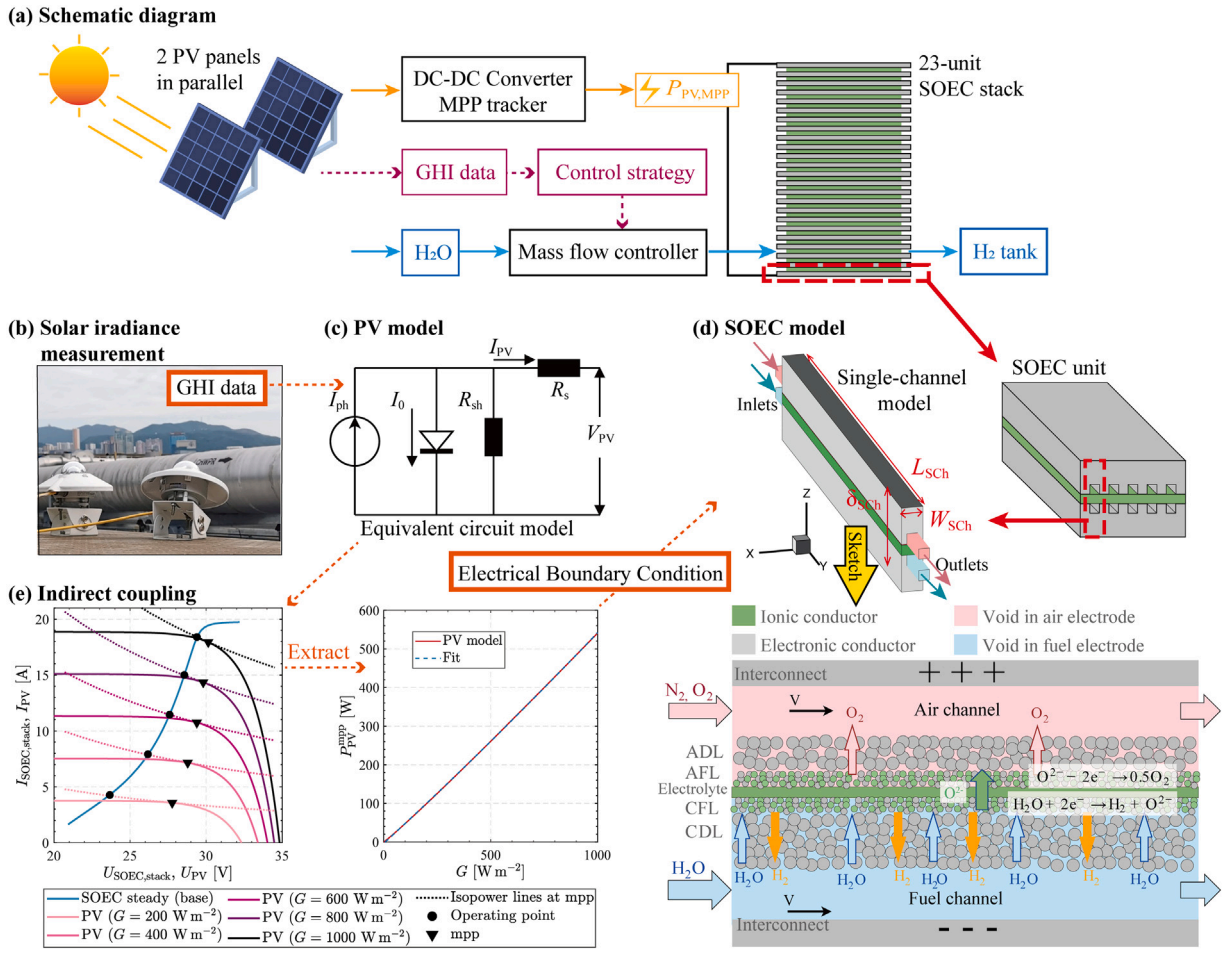

Fig. 1. Overview of the methodology used in this study. **a** The schematic diagram of the indirectly coupled PV-SOEC system. **b** Measurement of solar irradiance on a rooftop solar monitoring station located on our campus. **c** Equivalent circuit model of the PV system [29]. **d** The geometry and working principle of SOEC. **e** The indirect coupling between PV and SOEC. The images of PV panels in **a** are sourced from [30]; partial images in **d** are modified from our previous work [31,32].

- The ideal gas law is utilized for the calculation of fluid densities. Properties such as viscosity, specific heat and thermal conductivity, under ambient pressure, are sourced from the NIST database [36] and integrated into the model using piecewise linear interpolation.
- For solid materials, properties such as ionic, electronic, and thermal conductivities are assumed to be constant, except for the temperature-dependent ionic conductivity of the electrolyte. The effective properties of porous media are computed by volumetric averaging of the fluid and solid properties.

In this work, the boundary conditions (BC) used are presented in Table 1. The electrical BC is modified to allow the single-channel SOEC model to represent the coupling between the PV system and the SOEC stack. The detailed coupling method is explained in the following section.

2.4. Indirect coupling between PV and SOEC

The coupling between PV and electrolyzer can be classified into direct and indirect coupling [37]. In the case of direct coupling, the electrolyzer is directly linked to the photovoltaic system, implying that both systems operate at identical current and voltage. However, it poses a challenge to maintain their operating point proximate to the MPP of the PV, thereby reducing the efficiency of PV and the coupled system. To track the MPP of PV, the indirectly coupled PV-electrolyzer is integrated with an MPP tracker and a DC/DC converter [38], as shown in Figs. 1a and e. In this way, the PV can be operated at MPP under various conditions, and the power transmitted to the electrolyzer approximates the maximum power output of the PV. Therefore, in this work, the indirect coupling approach is selected.

The PV-SOEC system, as shown in Fig. 1a, includes 2 PV panels connected in parallel ($n_p^{PV} = 2$) and an SOEC stack composed of 23 SOEC units connected in series ($n_s^{SOEC} = 23$). As illustrated in Fig. 1e, the numbers of PV panels and SOEC units are tuned to ensure that the SOEC system approximates 90% of its maximum current when the PV is operating under $G = 1000\,\mathrm{W\,m^{-2}}$. The maximum power output of the PV system is configured to equal the power input of the SOEC system,

$$P_{SOEC,stack} = P_{PV}^{MPP}. \tag{7}$$

In Fig. 1e, the steady-state operating point of the PV-SOEC system is depicted as the intersection between the SOEC current–voltage curve and the iso-power line of the PV system.

In the SOEC stack, each individual SOEC unit consists of five parallel channels, with a total active area of $10\,\mathrm{cm^2}$ ($A_{act}^{SOEC,unit} = 10\,\mathrm{cm^2}$). That said, the SOEC single-channel model has an active area of $2\,\mathrm{cm^2}$ ($A_{act}^{SOEC,SCh} = 2\,\mathrm{cm^2}$). To apply the electrical conditions from the stack level to the single-channel model, the following equation is used,

$$I_{SOEC,SCh} = I_{SOEC,unit} \cdot \frac{A_{act}^{SOEC,SCh}}{A_{act}^{SOEC,unit}} = \frac{P_{SOEC,stack}}{U_{SOEC,stack}} \cdot \frac{A_{act}^{SOEC,SCh}}{A_{act}^{SOEC,unit}} = \frac{P_{SOEC,stack}}{n_s^{SOEC} U_{SOEC,unit}} \cdot \frac{A_{act}^{SOEC,SCh}}{A_{act}^{SOEC,unit}}. \tag{8}$$

Table 1
Boundary conditions of the numerical model utilized in this work. Note that the operating pressure is $p_0 = 1$ atm.

	Inlet[a]	Outlet	$x = 0$, $x/W_{SCh} = 1$	$z = 0$	$z/\delta_{SCh} = 1$	Other surfaces
Momentum	Base: $V_{in}^{air} = 2$, $V_{in}^{fuel} = 2$ Strategy A: $V_{in}^{air} = 10$, $V_{in}^{fuel} = 2$ Strategy B: $V_{in}^{air} = 2$, V_{in}^{fuel} = Eq. (14) Strategy C: $V_{in}^{air} = 2$, V_{in}^{fuel} = Eq. (15)	$p_{gauge} = 0$	Zero flux	N.A.	N.A.	$V = 0$
Thermal	$T_{in} = 1073$ K	O.B.	Zero flux	Zero flux	Zero flux	Zero flux
Species	$X_{in}^{O_2} = 0.2$, $X_{in}^{N_2} = 0.8$, $X_{in}^{H_2O} = 0.9$, $X_{in}^{H_2} = 0.1$	O.B.	Zero flux	N.A.	N.A.	Zero flux
Electrical	N.A.	N.A.	Zero flux	$\phi_{ele} = 0$	$i_{SOEC,SCh}$[b]	Zero flux

[a] The cell encompasses two inlets: the fuel channel inlet and the air channel inlet. The fuel inlet solely comprises H_2O and H_2, while the air inlet only comprises O_2 and N_2. Controlling SOEC operation is achieved by manipulating the inlet velocity [m s^{-1}].

[b] The electric current density i on the surface is a time-dependent function that ensures that the maximum power output of the PV system is equal to the power input of the SOEC stack under fluctuating solar conditions. The details are introduced in Section 2.4.

∗ This numerical study compares four different control strategies applied to V_{in}, with all other boundary conditions kept constant. O.B. means 'open boundary'. N.A. means 'not applicable'.

Then, the current density applied on the SOEC single-channel model can be computed as

$$i_{SOEC,SCh} = \frac{I_{SOEC,SCh}}{A_{act}^{SOEC,SCh}}. \tag{9}$$

Combining Eqs. (6)–(9), the electrical BC ($i_{SOEC,SCh}$) of the SOEC model listed in Table 1 is determined. This BC is incorporated in Ansys Fluent by User Defined Function (UDF).

The electrical efficiency of the SOEC is calculated as [3,39],

$$\begin{aligned}\text{Electrical efficiency} &= \frac{\text{Power consumed by electrolysis}}{\text{Power input of SOEC}} \\ &= \frac{|\Delta G_f^0| \cdot (I_{SOEC,unit} \cdot n_s^{SOEC})/(nF)}{P_{SOEC,stack}} \\ &= \frac{n_s^{SOEC} \cdot I_{SOEC,unit} \cdot |\Delta G_f^0|/(nF)}{n_s^{SOEC} \cdot I_{SOEC,unit} \cdot U_{SOEC,unit}} = \frac{U_{eq}^0}{U_{SOEC,unit}},\end{aligned} \tag{10}$$

where, $\Delta G_f^0 = -237.14 \times 10^3$ J mol^{-1} is the standard Gibbs free energy change of water formation, $n = 2$ is the number of participating electrons for hydrogen production, $F = 96485$ C mol^{-1} is the Faraday constant, $U_{eq}^0 = 1.229$ V is the equilibrium potential at standard condition [39].

The hydrogen production rate is,

$$\dot{Q}_{H2} = \frac{3600 \cdot I_{SOEC,stack} M_{H2}}{nF\rho_{H2}^0}, \tag{11}$$

where, $\dot{Q}_{H2}$ is the hydrogen production rate with unit L h^{-1}, $M_{H2} = 0.002$ kg mol^{-1} is the molar mass of hydrogen, $\rho_{H2}^0 = 89.88$ kg L^{-1} is the hydrogen density under the standard condition.

2.5. Control strategies of SOEC

Wang et al. [9] suggested that keeping the magnitudes of temperature gradient and temperature variation rate below 5 K cm^{-1} and 1 K min^{-1} respectively could reduce the failure probability of SOEC. In this study, the average temperature gradient is defined as

$$\text{Temperature gradient} = \frac{T_{out} - T_{in}}{L_{SCh}}, \tag{12}$$

where, T_{out} and T_{in} are the temperatures at the outlet and inlet of channel, and L_{SCh} denotes the length of the cell channel. Considering that the extreme temperature values within the SOEC typically appear near the inlet and outlet in the co-flow configuration [8] and thermally insulated boundary conditions, as shown in Fig. 3, the temperature gradient defined by Eq. (12) effectively captures the stream-wise average temperature gradient across the SOEC.

The temperature variation rate is defined as

$$\text{Temperature variation rate} = \frac{T_{ave}^n - T_{ave}^{n-1}}{\Delta t}, \tag{13}$$

where, the T_{ave}^n denotes the average temperature of SOEC at the nth step. The Δt is the simulation time step.

Increasing air flow rate, denoted as Strategy A in this work (Table 1), is a popular temperature control strategy proposed in the literature [13]. In Strategy A, the air flow rate is increased by five times compared to the base case. This strategy serves as a benchmark representing conventional control approaches. Strategies B and C adaptively control the steam flow rate to stabilize the internal heat source in SOEC according to the instantaneous solar power level. The objectives of Strategies B and C are to maintain SOEC at states of thermal neutrality (TN) and slight endothermicity (the temperature gradient of -3 K cm^{-1}), respectively. For strategies B and C, the correlations between the steam velocity in the fuel channel and the input power are numerically regressed as (see Section 3.3.3 for more details)

$$\text{Strategy B: } V_{in}^{fuel} = 0.3873 \cdot P_{SOEC,SCh} - 0.0326, \tag{14}$$

$$\text{Strategy C: } V_{in}^{fuel} = 0.0179 \cdot P_{SOEC,SCh}^2 + 0.323 \cdot P_{SOEC,SCh} + 0.0355. \tag{15}$$

3. Result and discussion

3.1. Guidance from the transient characteristics of PV-SOEC

Before delving into our heat source-based control strategies, we conducted a simulation to explain the transient characteristics of the PV-SOEC system in response to a sudden change in solar irradiance. The transient characteristics will provide guidance for control strategies.

In an indirectly coupled PV-SOEC system, fluctuations in solar irradiance can affect the power supply to the SOEC. These changes in the electrical state can, in turn, alter the heat and mass fields within the SOEC. In simulation, GHI undergoes a rapid ramp-down, characterized as a linear decrease from 1000 to 200 W m^{-2} in 1 ms, and hold constant at 200 W m^{-2}. The simulation adopted an adaptive time-step size to accurately capture the responses of SOEC [31]. The BCs of the SOEC are presented as the base case in Table 1. The animation of electrical responses of the coupled system is provided in the Supplementary Video S1. Fig. 2 depicts the electrical, gaseous, and thermal responses of SOEC to the sudden change in irradiance. Although electrical parameters (including current, voltage, and power) can adapt quickly to the GHI rampdown, the gaseous response is slower, persisting for approximately 0.1 s. The slowest response is that of temperature, which takes thousands of seconds to reach a new steady state. These differential speeds of electrical, gaseous, and thermal responses were previously discussed in our previous studies [31,32]. In light of the response speeds, fast response factors, such as current and gas flow rates, can be employed to control slow response factors, such as temperature. To adapt to highly fluctuating solar power, effective operating strategies for temperature control should be based on the fast-response factors such as current and gas flow rates.

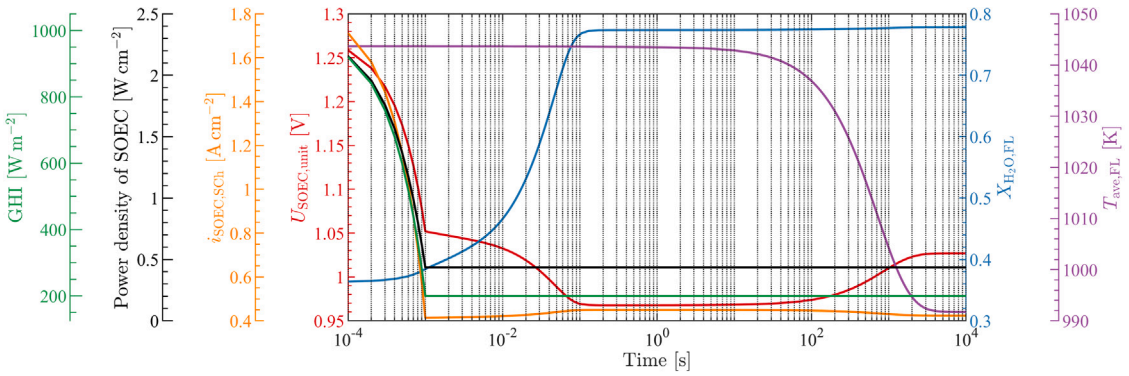

Fig. 2. Responses of the single-channel SOEC model to a rapid ramp-down in GHI from 1000 to 200 W m^{-2} for a coupled PV-SOEC system. The power density, current density ($i_{SOEC,SCh}$), and voltage ($U_{SOEC,unit}$) variations with respect to time are illustrated. The time-varying average mole fraction of H_2O ($X_{H_2O,FL}$) and average temperature ($T_{ave,FL}$) in the functional layers are also presented.

Fig. 2 also shows a significant temperature drop of around 50 K following the decrease in GHI. Fig. 3b–c compare the steady-state temperature distributions of the initial and final states of Fig. 2. The temperature drop originates from the decrease of the total heat source within the SOEC. Additionally, the negative total heat source induces temperature gradients within the SOEC. To reduce the probability of failure of the SOEC, it is vital to examine control strategies that can effectively manage the temperature gradient and variation of the SOEC.

3.2. Limitations of conventional control strategies based on air flow rate

As discussed in Section 3.1, gas flow rate is a factor that has sufficiently fast response dynamics for the temperature control of SOEC. The strategy of controlling air flow rate has been widely adopted in the literature [13–15,17,18]. However, this control strategy shows limited performance for SOEC temperature control under severe power fluctuations [9]. In this section, we use steady simulations to analyze the limitations of controlling air flow rate and point out the importance of controlling the internal heat source.

Fig. 3c–f illustrate that, as the air velocity increases from 2 to 30 m s^{-1}, the values of the total heat sources show a slight difference, while the overall temperature of the SOEC increases significantly and the temperature gradient decreases. These observations, on the one hand, suggest that increasing air flow rate is an effective strategy for reducing the temperature gradient. On the other hand, the thermal effect of increasing the air flow rate is similar to the 'dilution' of the endothermic effect, without drastically altering the internal heat source within the SOEC. However, when the magnitude of the heat source is large, a considerably high air flow rate is needed to dilute the heat source to ensure an acceptable temperature gradient [9]. This, in turn, necessitates substantial compressor work and rigorous gas-tight sealing of the SOEC.

To better understand temperature control strategies, the SOEC can be considered as a control volume, as shown in Fig. 3a. Steam and air flows represent heat flux across the boundaries of the control volume. Within the control volume, electrochemical reactions and Joule heating function as an internal heat source S_H. Upon reaching a thermal steady state within the control volume, the heat source is equal to the enthalpy difference between the heat fluxes

$$0 = \dot{\mathcal{H}}_0 - \dot{\mathcal{H}} + S_H = \bar{\rho}\bar{c}_p\dot{\mathcal{V}}_{ave}(T_{in} - T_{out}) + S_H, \tag{16}$$

where $\dot{\mathcal{H}}_0$ and $\dot{\mathcal{H}}$ denote the enthalpy flow rates at the inlet and outlet, respectively. $\bar{\rho}$, $\bar{c}_p$, and $\dot{\mathcal{V}}_{ave}$ denote the average density, specific heat capacity, and volumetric flow rate of gases through the SOEC. The temperature difference between inlet and outlet can be further expressed as

$$\Delta T_{in,out} = T_{out} - T_{in} = \frac{S_H}{\bar{\rho}\bar{c}_p\dot{\mathcal{V}}_{ave}}. \tag{17}$$

Eq. (17) indicates the two general control strategies to reduce temperature difference $\Delta T_{in,out}$: one is to increase $\dot{\mathcal{V}}_{ave}$, and the other is to reduce S_H. The conventional control strategy based on air flow rate is equivalent to the adjustment of $\dot{\mathcal{V}}_{ave}$. When S_H is high, adjusting $\dot{\mathcal{V}}_{ave}$ shows a reduced performance to constrain $\Delta T_{in,out}$ within SOEC due to the low specific heat capacity c_p of air [9]. To effectively constrain $\Delta T_{in,out}$, it is important to develop a control strategy that can control the heat source S_H in SOEC.

3.3. Derivation of heat source-based control strategies

3.3.1. Determination of key variables for controlling heat source

In SOECs, the heat source is coupled with electrical power and electrochemical reactions. An in-depth understanding of the energy balance can facilitate the identification of key variables to control the heat source. As shown in Fig. 4, the electrochemical processes in SOEC can be idealized as a one-step water-splitting reaction at constant temperature. The amount of energy required for the water-splitting reaction is $I|\Delta\mathcal{H}_f|/nF$. Here, $\Delta\mathcal{H}_f$ is the enthalpy of the formation of water [40]

$$\Delta\mathcal{H}_f = \Delta G + T\Delta S_f, \tag{18}$$

where, ΔG is the change of Gibbs free energy, which is the minimum electrical energy required for electrolysis. ΔS_f is the entropy of water formation. The values of $\Delta\mathcal{H}_f$, ΔG, and ΔS_f depend on the thermodynamic properties of the reactants and products.

The water-splitting reaction acquires energy from the electrical power source ($I\Delta G/nF$) and the thermal environment ($IT|\Delta S_f|/nF$). Besides, the excess electrical power ($I\eta_{total}$) input to SOEC is dissipated as heat, where η_{total} signifies the total overpotential that depends on electrochemical kinetics, Ohmic resistances, and the operational conditions of SOEC. By examining the thermal energy balance, the total heat source S_H of SOEC can be determined,

$$S_H = I\eta_{total} - I\frac{T|\Delta S_f|}{nF}. \tag{19}$$

The sign and magnitude of S_H determine the thermal behavior of the SOEC. From Eq. (19) and Fig. 4, we identify four variables that can be adjusted to control the magnitude of the heat source:

- Reaction pathway. SOEC can accommodate different fuels [5]. By supplying different reactants, such as steam and carbon dioxide mixture, the $\Delta\mathcal{H}$ and ΔS of reaction within the SOEC can be regulated [20].
- Temperature [23,26]. Temperature has wide-ranging effects on factors such as the Ohmic resistance of the solid electrolyte, current, voltage, and enthalpy change. However, as discussed in Section 3.1, the temperature responds more slowly than gas and

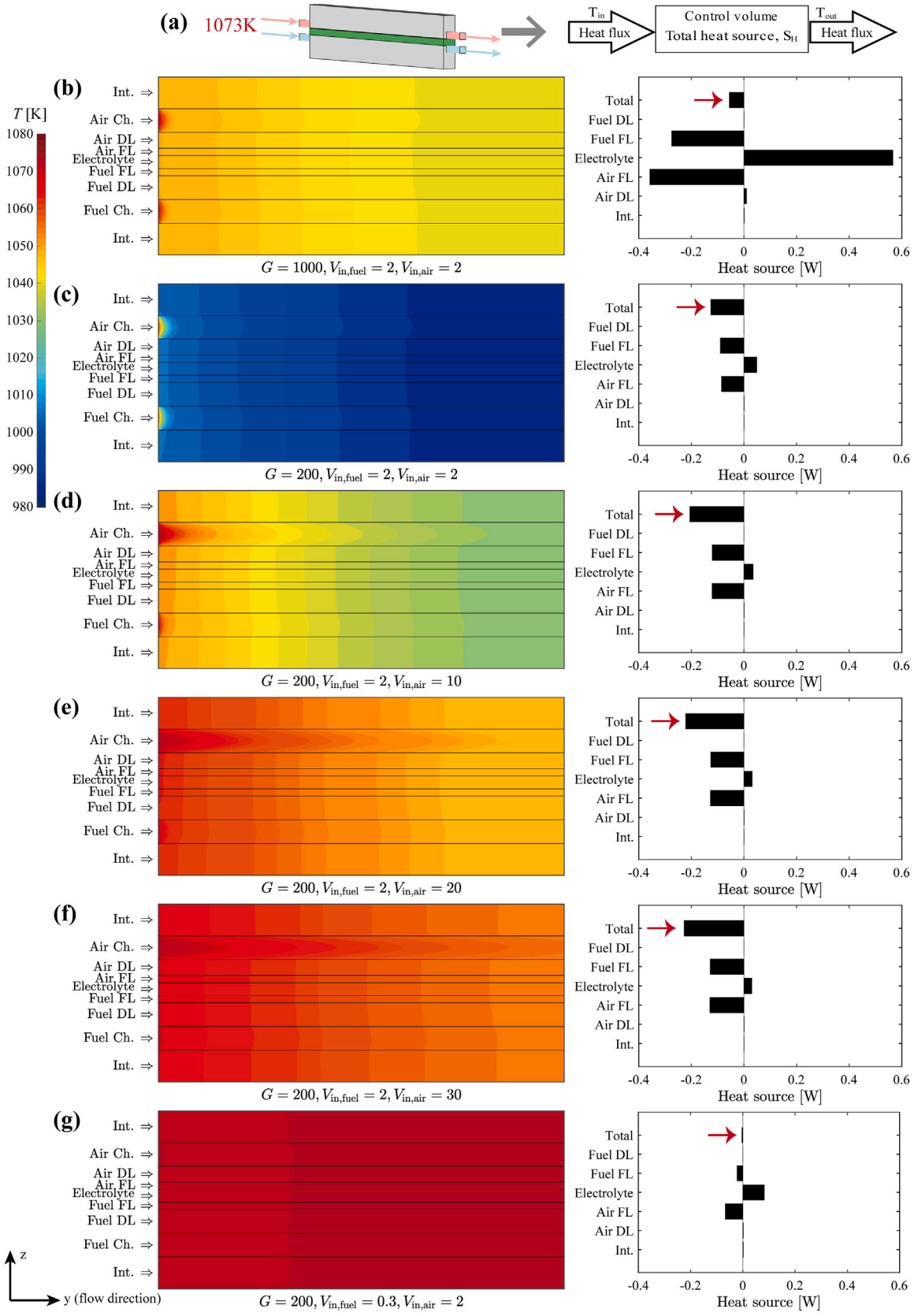

Fig. 3. Heat transfer within SOEC. **a** Energy conservation of the control volume. **b–g** Distributions of temperature (left panel) and heat source (right panel) in steady state with different solar irradiance (G [$\mathrm{W\,m^{-2}}$]) and inlet velocities of air and fuel channels ($V_{\mathrm{in,air}}$, $V_{\mathrm{in,fuel}}$ [$\mathrm{m\,s^{-1}}$]). The length scales of SOEC have been adjusted in this figure for better visualization.

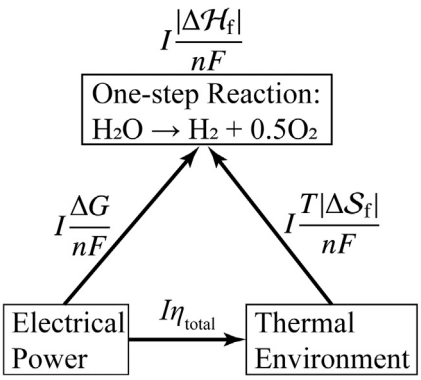

Fig. 4. Energy balance in SOEC, which is simplified to one-step reaction.

electricity [22,31]. Thus, it might be challenging to regulate the heat source by only manipulating the temperature field, especially under conditions of highly fluctuating power.

- Current I. The change in current will vary the overpotential η_{total}. The net current flowing through the system can be controlled by adjusting the series and parallel connections of the SOEC units during operation [41,42]. This, in turn, allows for the regulation of the heat source.
- Inlet flow rate of the reactant. The maximum achievable current is limited by the supply of reactants in SOEC. Thus, we can control the heat source by adjusting the flow rate of the reactant. The limiting current (I_{lim}) is presented as

$$I \le I_{lim} = \frac{nFp_0 X_{in}^{H_2O} A_{ch} V_{in}^{fuel}}{\mathcal{R}T_{in}}, \tag{20}$$

where, $A_{ch} = 10^{-6}\,m^2$ is the cross area of fluid channel, $\mathcal{R} = 8.314\,J\,mol^{-1}\,K^{-1}$ is the ideal gas constant.

Considering the applicability of control strategies and the fast-response dynamics of gases (Section 3.1), we propose to only adjust the inlet steam velocity in the fuel channel (V_{in}^{fuel}) to continuously neutralize the heat source within the SOEC under varying power supply.

3.3.2. Theoretical feasibility of thermoneutral control strategy

Theoretically, by adjusting V_{in}^{fuel}, the SOEC can be maintained at thermal neutrality for high thermal uniformity. Based on Eq. (19), SOEC achieves thermal neutrality ($S_H = 0$) when

$$\eta_{total} = \frac{T|\Delta S_f|}{nF}. \tag{21}$$

Then, based on Fig. 4, the theoretical electrical power required to maintain SOEC at thermal neutrality can be expressed as

$$P_{SOEC}^{theo} = I\frac{\Delta G}{nF} + I\eta_{total} = I\frac{\Delta G}{nF} + I\frac{T|\Delta S_f|}{nF} = I\frac{|\Delta\mathcal{H}_f|}{nF} = IU_{TN}^{theo}. \tag{22}$$

Consequently, the theoretical thermoneutral voltage U_{TN}^{theo} for the water-splitting reaction [43] is derived as

$$U_{TN}^{theo} = \frac{|\Delta\mathcal{H}_f|}{nF}. \tag{23}$$

According to the NIST database [36], at the ambient pressure and the temperature of 1073 K, the values of $\Delta\mathcal{H}_f$ and U_{TN}^{theo} for water are $-246.4\,kJ\,mol^{-1}$ and 1.28 V, respectively.

To theoretically derive the thermoneutral control strategy, a high conversion rate of reactant H_2O is assumed at the thermal neutrality of SOEC and hence the current approximates the limiting current,

$$I \approx I_{lim}. \tag{24}$$

Combining Eqs. (20)–(24), the thermoneutral control strategy based on V_{in}^{fuel} is theoretically derived,

$$V_{in,TN}^{fuel} \approx \frac{\mathcal{R}T_{in}}{nFp_0 X_{in}^{H_2O} A_{ch} U_{TN}^{theo}} P_{SOEC}^{theo}. \tag{25}$$

Given the values of T_{in}, $X_{in}^{H_2O}$, and p_0 in Table 1, Eq. (25) can be written as a linear formula,

$$V_{in,TN}^{fuel} \approx 0.3961 \cdot P_{SOEC}^{theo}. \tag{26}$$

3.3.3. Acquisition of heat source-based control strategies

Eq. (25) determines the theoretical feasibility of neutralizing the heat source within the SOEC by adjusting V_{in}^{fuel} under different power inputs. However, the theoretical derivation is based on assumptions such as Eq. (24). Thus, $V_{in,TN}^{fuel}$ calculated from Eq. (26) cannot exactly lead to the thermal neutrality of SOEC in reality, but gives the initial guess of the actual $V_{in,TN}^{fuel}$. Based on the initial guess, the V_{in}^{fuel} to achieve thermal neutrality ($\Delta T_{in,out} = 0, S_H = 0$) for different GHI levels is inferred by performing a number of steady state numerical simulations of the PV-SOEC system, as shown in Fig. 5(a). Subsequently, the relationship between the thermoneutral flow rate $V_{in,TN}^{fuel}$ and the input power $P_{SOEC,SCh}$ is linearly regressed, as shown in Fig. 5(b) and presented in Eq. (14). The thermoneutral control strategy, Eq. (14), is adopted as the Strategy B in this study. Furthermore, Fig. 5(b) shows that the theoretically derived Eqs. (25)–(26) can not only provide a good guess of $V_{in,TN}^{fuel}$ but also serve as an indicator for the thermal states of SOEC. Given a value of $P_{SOEC,SCh}$, SOEC is endothermic at a steam velocity greater than $V_{in,TN}^{fuel}$ and exothermic below it. Eq. (25) exhibits its ease and effectiveness in guiding the SOEC operational design.

With Eq. (14), we can control V_{in}^{fuel} to neutralize the heat source within the SOEC under variable solar conditions in numerical simulation. For example, when $G = 200\,W\,m^{-2}$, the power applied on the single-channel SOEC model is 0.87 W. Then, adjusting V_{in}^{fuel} to 0.3 m/s as calculated using Eq. (14) could maintain the total internal heat source at around zero. As shown in Fig. 3g, the adjustment on the V_{in}^{fuel} leads to a highly uniform temperature distribution within the SOEC, indicating the effectiveness of the proposed strategy.

Alternatively, by adjusting the steam flow rate, SOEC can be maintained slightly endothermic for higher electrical efficiency. In this study, Strategy C is designed to maintain a slight temperature gradient of $-3\,K\,cm^{-1}$ within the SOEC, as shown in Fig. 5(a). Such temperature gradient is acceptable as it falls within the suggested magnitude of $5\,K\,cm^{-1}$ [9,21]. To develop Strategy C, the relationship between the steam flow rate V_{in}^{fuel} and the input power $P_{SOEC,SCh}$ is regressed at $\Delta T_{in,out}/L_{SCh} = -3\,K\,cm^{-1}$, as presented in Eq. (15).

3.4. Controlling heat source in SOEC under fluctuating solar conditions

Effectiveness of temperature control

Fig. 6 shows the comparison of four different operating strategies for the SOEC under fluctuating solar irradiance. The one-hour GHI data with a temporal resolution of 2 s collected in Hong Kong from 11:59:10 to 12:59:10 on August 30th, 2023, serve as input for the coupled PV-SOEC model. Transient simulations were performed with a constant timestep of 2 s. The four operating strategies applied on the SOEC are detailed in Table 1. The base case refers to a scenario with constant operating parameters. In Strategy A, the air flow rate is increased to five times that of the base case. Strategies B and C manipulate the steam velocity according to GHI using Eqs. (14)–(15), aiming to maintain SOEC at states of thermal neutrality and slight endothermicity (the temperature gradient of $-3\,K\,cm^{-1}$), respectively. All four cases are initialized with the same condition, which is the steady-state solution with the base case settings when $G = 1000\,W\,m^{-2}$.

Fig. 6a presents the measured GHI data and the corresponding sky images. During the study period, dynamic cloud fields result in significant fluctuations in GHI, ranging from about 1000 to 200 $W\,m^{-2}$

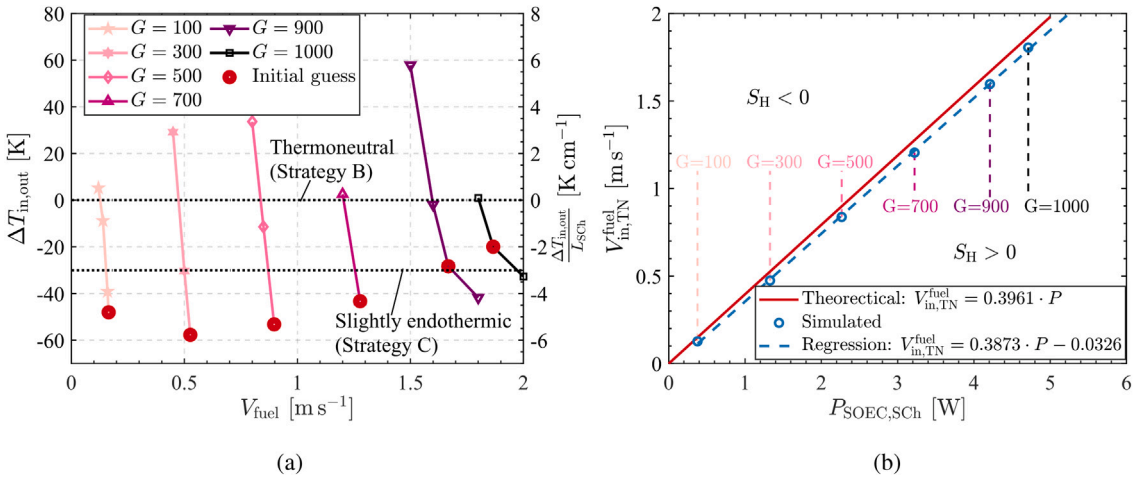

Fig. 5. Steam velocity of fuel channel to achieve thermal neutrality in SOEC under different GHI (G [W m^{-2}]). (a) Temperature difference with respect to $V^{\mathrm{fuel}}_{\mathrm{in}}$ and G. The intersects between the color lines and the two dotted lines are the $V^{\mathrm{fuel}}_{\mathrm{in}}$ that could maintain the SOEC at the thermoneutral or slight endothermic state. (b) The thermoneutral $V^{\mathrm{fuel}}_{\mathrm{in}}$ with respect to power input of SOEC.

within the hour. The corresponding functions in the PV power are presented in Fig. 6b. As shown in Fig. 6c, the oscillating solar irradiance induces a temperature gradient within the SOEC in the base case. This gradient exceeds the recommended limit of 5 K cm^{-1} [9,21] during periods of high solar variability. For Strategy A, increasing the air flow rate can reduce the temperature gradient to below the suggested limit. For Strategy B, by manipulating the steam velocity according to solar power, the temperature is regulated towards thermal neutrality, and the temperature gradient is nearly eliminated. Strategy C also successfully maintains the SOEC in a slightly endothermic state with a safe temperature gradient of around -3 K cm^{-1}.

Fig. 6d compares the variation rates of the average SOEC temperature in the four cases. The temperature variation rates in the base case and Strategy A are heavily influenced by GHI fluctuations and frequently exceed the recommended limit of 1 K min^{-1} [9]. These rates even exceed 5 K, min^{-1} at certain times, such as at 12:07, 12:15, and 12:28. Such high temperature variation rates can induce thermal fatigue and increase the likelihood of SOEC failure. For Strategy B, the temperature variation rate exceeds 1 K min^{-1} within the initial 7 min due to an overshoot of the heat source, as shown in Fig. 6e. Afterwards, the SOEC operates safely and stably within the limit. In general, in Strategies B and C, the control of the steam velocity successfully reduces the rate of temperature variation to below the suggested limit of 1 K min^{-1}.

The effectiveness of Strategies B and C is demonstrated by Fig. 6e, which compares the total heat sources within the SOEC. For the base case, the heat source within the SOEC is highly sensitive to fluctuating solar power. large-amplitude variations in the heat source lead to rapid temperature changes. Strategy A is unable to maintain the rate of temperature change within the recommended limits by merely increasing the air flow rate. In contrast, Strategies B and C achieve success in managing the heat source by adjusting the steam flow rate of SOEC. On the one hand, they suppress large-amplitude variations of the heat source, resulting in a reduced rate of temperature change. On the other hand, they maintain the magnitude of the heat source at a low level, which contributes to a small temperature gradient within the SOEC.

In addition, the slow temperature regulation process of SOEC should be highlighted in Fig. 6c. Due to the regulation of Strategy B, the outlet temperature T_{out} of SOEC increases from the initial state of 1040 K to the thermoneutral point of 1073 K. The temperature increase lasts for approximately 20 min. This long time required for SOEC temperature regulation is also observed by Aguiar et al. [18]. We propose that the considerable time for temperature regulation is associated with the characteristic time of heat transfer of the SOEC [32], which represents the time necessary for the SOEC to achieve a new thermal equilibrium after a variation of the heat source. In our previous work [32], we have explained the physics of the long time for temperature regulation through Eq. (27), which is comparable to the time required for heat fluxes to 'fill' the heat capacity of SOEC. Eq. (27) can be used to estimate the characteristic time of heat transfer, where, $\dot{H}$ is the enthalpy flow rate, m is mass and $\dot{m}$ is mass flow rate. The subscripts 'E', 'int', and 'ch' correspond to the electrolyte, the interconnect, and the fluid channel, respectively. In Strategy B, the estimated characteristic time of heat transfer is 1100 s, which is closely aligned with the simulated temperature regulation time for Strategy B. This indicates a correlation between the slow temperature regulation process and the heat-transfer characteristic time of SOEC.

Comparison of efficiencies

Although Strategy B exhibits superior uniformity of temperature and thermal stability, it shows an electrical efficiency of 91.2%, lower than the 100.7% of base case and the 103.0% of Case 1, as shown in Fig. 6f. Interestingly, at low GHI, the efficiency of Strategy B decreases, while the efficiency of the base case and Case 1 can increase to even higher than 100%. This phenomenon is attributed to the energy utilization of the SOEC. Given a low GHI, such as 400 W m^{-2}, the base case and Strategy A exhibit reduced voltages due to the low solar power and the electrical characteristics of SOEC (see Fig. 1e), while Strategy B maintain the voltages at high levels. According to Eq. (10), a lower voltage correlates with an increase in electrical efficiency. This relationship elucidates the higher efficiencies observed in the base case and Strategy A, in contrast to the lower efficiency of Strategy B. However, the high electrical efficiency necessitates significant heat absorption from the surrounding environment to compensate for the reduced electrical energy consumption. Thus, the strategy demonstrating high electrical efficiency leads to strong endothermic effects and temperature gradient, as shown in Fig. 6c, e, and f. This situation reveals an inherent contradiction between temperature control and the maximization of efficiency. Strategy C presents a solution to this dilemma by operating the SOEC in a slightly endothermic state, achieving an electrical efficiency of 94.9%. Compared to thermal neutrality, the slight endothermicity allows for an acceptable temperature gradient within SOEC (< 5 K cm^{-1}) while maintains the high electrolysis efficiency.

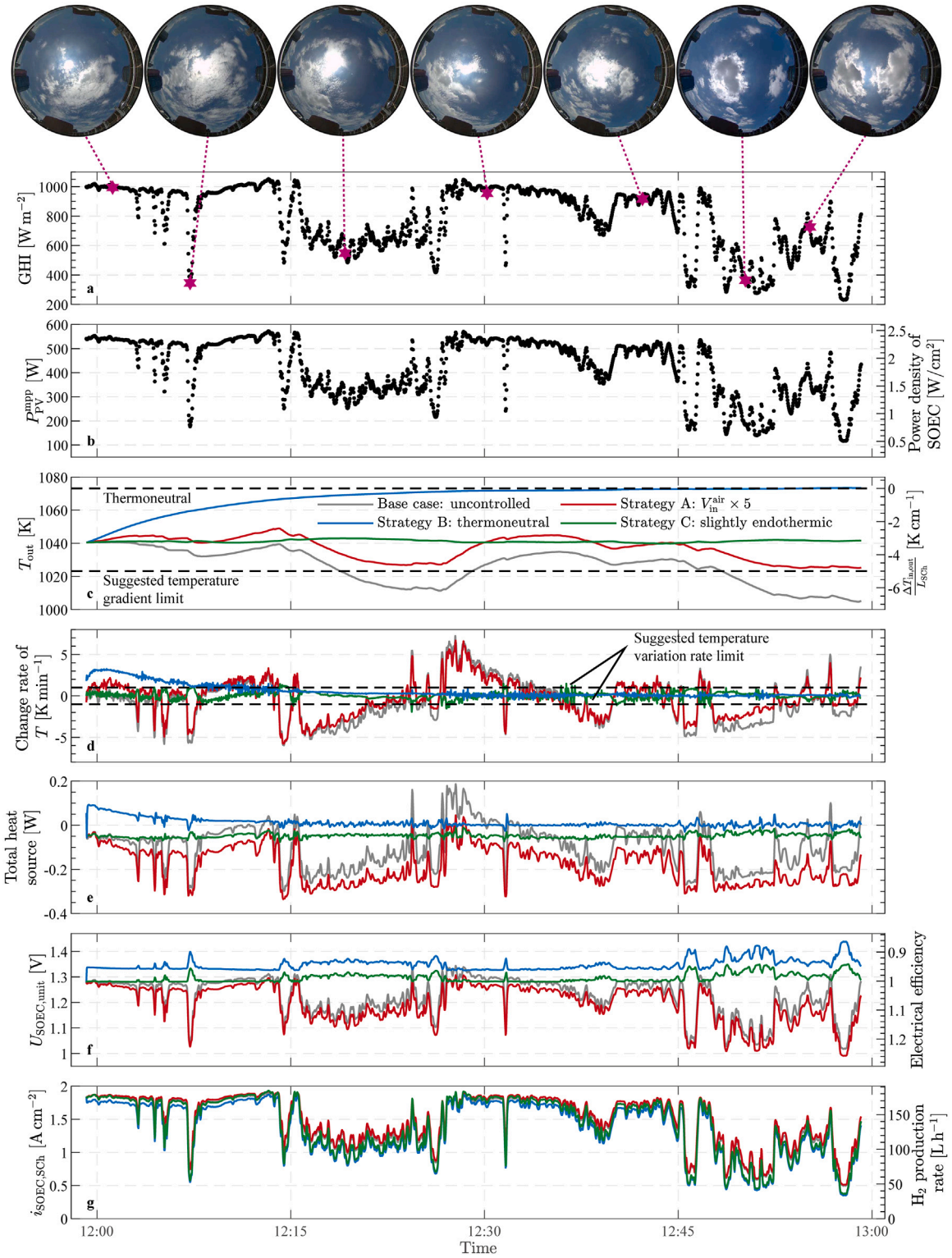

Fig. 6. Comparison of four different operating strategies on the PV-SOEC system under fluctuating solar irradiance. (a) shows the one-hour GHI data and sky image. (b) presents the maximum power output from PV system and the power density applied on SOEC. The variables for comparison includes: (c) outlet temperature and temperature gradient, (d) temperature variation rate, (e) the total heat source within the single-channel SOEC model, (f) voltage and electrical efficiency, and (g) current density and hydrogen production rate.

Fig. 6g provides an additional comparison of currents and the hydrogen production rate in the four cases. Based on Eq. (11), the average hydrogen production rates for the base case and Strategies A–C are 140.9 L h^{-1}, 144.1 L h^{-1}, 130.4 L h^{-1}, and 135.5 L h^{-1}. This outcome further illustrates that the operation of SOEC at a slight endothermicity can effectively balance thermal management and system efficiency.

$$\tau_{\mathrm{h}} = \frac{\text{Total enthalpy}}{\text{Total heat transfer rate}}\ \frac{[\mathrm{J}]}{[\mathrm{W}]} = \frac{\mathcal{H}_{0,\mathrm{int}}^{\mathrm{solid}} + \mathcal{H}_{0,\mathrm{E}}^{\mathrm{solid}} + \mathcal{H}_{0,\mathrm{AFL}}^{\mathrm{eff}} + \mathcal{H}_{0,\mathrm{ADL}}^{\mathrm{eff}} + \mathcal{H}_{0,\mathrm{CDL}}^{\mathrm{eff}} + \mathcal{H}_{0,\mathrm{CFL}}^{\mathrm{eff}} + \mathcal{H}_{0,\mathrm{ch}}^{\mathrm{fluid}}}{\dot{\mathcal{H}}_{\mathrm{in}}^{\mathrm{fuel}} + \dot{\mathcal{H}}_{\mathrm{in}}^{\mathrm{air}}}$$
$$\approx \frac{(mc_p)_{0,\mathrm{int}}^{\mathrm{solid}} + (mc_p)_{0,\mathrm{E}}^{\mathrm{solid}} + (mc_p)_{0,\mathrm{AFL}}^{\mathrm{eff}} + (mc_p)_{0,\mathrm{ADL}}^{\mathrm{eff}} + (mc_p)_{0,\mathrm{CDL}}^{\mathrm{eff}} + (mc_p)_{0,\mathrm{CFL}}^{\mathrm{eff}} + (mc_p)_{0,\mathrm{ch}}^{\mathrm{fluid}}}{(\dot{m}c_p)_{\mathrm{in}}^{\mathrm{fuel}} + (\dot{m}c_p)_{\mathrm{in}}^{\mathrm{air}}}, \tag{27}$$

Box I.

4. Conclusion

To improve the thermal safety of SOEC when integrated with PV panels under fluctuating solar irradiance, theoretical analysis and numerical simulation are conducted to investigate the control strategies for SOEC. Recognizing that the maximum current of SOEC is intrinsically limited by the steam supply rate, we developed control strategies that adaptively adjust the steam velocity according to real-time solar power. In this way, the magnitude of the heat source within the SOEC can be maintained at a low level, ensuring that the temperature gradient and variation within SOEC remain below $5\,\mathrm{K\,cm^{-1}}$ and $1\,\mathrm{K\,min^{-1}}$, respectively, even under highly fluctuating solar power. This would enhance the durability and safety of SOEC when integrated with intermittent power sources.

In addition, we found that while the thermoneutral operation of SOEC shows superior temperature uniformity and stability, it lags behind the endothermic operations in terms of electrical efficiency, because it lacks the utilization of thermal energy to compensate for electrical energy. This observation indicates a contradiction between temperature uniformity and the maximization of efficiency in SOEC. To strike a balance for this contradiction, our control strategy can alternatively maintain the SOEC in a slight endothermic state for a high efficiency of 94.9% and an acceptable temperature gradient below $5\,\mathrm{K\,cm^{-1}}$ under fluctuating solar power.

CRediT authorship contribution statement

Zhaojian Liang: Writing – original draft, Software, Methodology, Investigation, Formal analysis, Conceptualization. **Shanlin Chen:** Writing – review & editing, Software, Methodology, Data curation. **Meng Ni:** Writing – review & editing. **Jingyi Wang:** Writing – review & editing, Visualization, Project administration, Funding acquisition. **Mengying Li:** Writing – review & editing, Supervision, Resources, Investigation, Funding acquisition.

Declaration of competing interest

The authors declare that they have no known competing financial interests or personal relationships that could have appeared to influence the work reported in this paper.

Data availability

Data will be made available on request.

Declaration of Generative AI and AI-assisted technologies in the writing process

During the preparation of this work, the authors used GPT-4 to improve language and readability. After using this tool, the authors reviewed and edited the content as needed and take full responsibility for the content of the publication.

Acknowledgment

The authors gratefully acknowledge the partial support from The Hong Kong Polytechnic University (P0035016), National Natural Science Foundation of China (No. 52306236), Science, Technology and Innovation Commission of Shenzhen Municipality (GXWD20220811165757005), and Department of Education of Guangdong Province, China (2021KQNCX271).

Appendix A. Supplementary data

Supplementary material related to this article can be found online at https://doi.org/10.1016/j.apenergy.2024.123669.

References

[1] Wang Y, Wu C, Zhao S, Guo Z, Han M, Zhao T, et al. Boosting the performance and durability of heterogeneous electrodes for solid oxide electrochemical cells utilizing a data-driven powder-to-power framework. Sci Bull 2023;68(5):516–27. http://dx.doi.org/10.1016/j.scib.2023.02.019.

[2] IEA. World energy outlook 2023. IEA Paris, France; 2023, URL https://www.iea.org/reports/world-energy-outlook-2023.

[3] Hu K, Fang J, Ai X, Huang D, Zhong Z, Yang X, et al. Comparative study of alkaline water electrolysis, proton exchange membrane water electrolysis and solid oxide electrolysis through multiphysics modeling. Appl Energy 2022;312:118788. http://dx.doi.org/10.1016/j.apenergy.2022.118788.

[4] Min G, Choi S, Hong J. A review of solid oxide steam-electrolysis cell systems: Thermodynamics and thermal integration. Appl Energy 2022;328:120145. http://dx.doi.org/10.1016/j.apenergy.2022.120145.

[5] Xu Q, Guo Z, Xia L, He Q, Li Z, Temitope Bello I, et al. A comprehensive review of solid oxide fuel cells operating on various promising alternative fuels. Energy Convers Manage 2022;253:115175. http://dx.doi.org/10.1016/j.enconman.2021.115175.

[6] Beale SB, Andersson M, Boigues-Muñoz C, Frandsen HL, Lin Z, McPhail SJ, et al. Continuum scale modelling and complementary experimentation of solid oxide cells. Prog Energy Combust Sci 2021;85:100902. http://dx.doi.org/10.1016/j.pecs.2020.100902.

[7] Petipas F, Fu Q, Brisse A, Bouallou C. Transient operation of a solid oxide electrolysis cell. Int J Hydrog Energy 2013;38(7):2957–64. http://dx.doi.org/10.1016/j.ijhydene.2012.12.086.

[8] Zeng Z, Qian Y, Zhang Y, Hao C, Dan D, Zhuge W. A review of heat transfer and thermal management methods for temperature gradient reduction in solid oxide fuel cell (SOFC) stacks. Appl Energy 2020;280:115899. http://dx.doi.org/10.1016/j.apenergy.2020.115899.

[9] Wang Y, Banerjee A, Deutschmann O. Dynamic behavior and control strategy study of CO2/H2O co-electrolysis in solid oxide electrolysis cells. J Power Sources 2019;412:255–64. http://dx.doi.org/10.1016/j.jpowsour.2018.11.047.

[10] Liu H, Høgh J, Blennow P, Sun X, Zong Y, Chen M. Assessing fluctuating wind to hydrogen production via long-term testing of solid oxide electrolysis stacks. Appl Energy 2024;361:122938. http://dx.doi.org/10.1016/j.apenergy.2024.122938.

[11] Sun Y, Lu J, Liu Q, Shuai W, Sun A, Zheng N, et al. Multi-objective optimizations of solid oxide co-electrolysis with intermittent renewable power supply via multi-physics simulation and deep learning strategy. Energy Convers Manage 2022;258:115560. http://dx.doi.org/10.1016/j.enconman.2022.115560.

[12] Xiao G, Sun A, Liu H, Ni M, Xu H. Thermal management of reversible solid oxide cells in the dynamic mode switching. Appl Energy 2023;331:120383. http://dx.doi.org/10.1016/j.apenergy.2022.120383.

[13] Liu G, Zhao W, Li Z, Xia Z, Jiang C, Kupecki J, et al. Modeling and control-oriented thermal safety analysis for mode switching process of reversible solid oxide cell system. Energy Convers Manage 2022;255:115318. http://dx.doi.org/10.1016/j.enconman.2022.115318.

[14] Udagawa J, Aguiar P, Brandon N. Hydrogen production through steam electrolysis: Model-based dynamic behaviour of a cathode-supported intermediate temperature solid oxide electrolysis cell. J Power Sources 2008;180(1):46–55. http://dx.doi.org/10.1016/j.jpowsour.2008.02.026.
[15] Zhang B, Maloney D, Farida Harun N, Zhou N, Pezzini P, Medam A, et al. Rapid load transition for integrated solid oxide fuel cell – gas turbine (SOFC-GT) energy systems: A demonstration of the potential for grid response. Energy Convers Manage 2022;258:115544. http://dx.doi.org/10.1016/j.enconman.2022.115544.
[16] Zhu P, Wu Z, Yang Y, Wang H, Li R, Yang F, et al. The dynamic response of solid oxide fuel cell fueled by syngas during the operating condition variations. Appl Energy 2023;349:121655. http://dx.doi.org/10.1016/j.apenergy.2023.121655.
[17] Botta G, Romeo M, Fernandes A, Trabucchi S, Aravind P. Dynamic modeling of reversible solid oxide cell stack and control strategy development. Energy Convers Manage 2019;185:636–53. http://dx.doi.org/10.1016/j.enconman.2019.01.082.
[18] Aguiar P, Adjiman C, Brandon N. Anode-supported intermediate-temperature direct internal reforming solid oxide fuel cell: II. Model-based dynamic performance and control. J Power Sources 2005;147(1):136–47. http://dx.doi.org/10.1016/j.jpowsour.2005.01.017.
[19] Lu B, Zhang Z, Zhang Z, Zhang C, Zhu L, Huang Z. Control strategy of solid oxide electrolysis cell operating temperature under real fluctuating renewable power. Energy Convers Manage 2024;299:117852. http://dx.doi.org/10.1016/j.enconman.2023.117852.
[20] Liu G, Wang Z, Liu X, Kupecki J, Zhao D, Jin B, et al. Transient analysis and safety-oriented process optimization during electrolysis–fuel cell transition of a novel reversible solid oxide cell system. J Clean Prod 2023;425:139000. http://dx.doi.org/10.1016/j.jclepro.2023.139000.
[21] Chen H, Wu T, Luo S, Wang Y, Xu X. Operating strategy investigation of a solid oxide electrolysis cell under large scale transient electrical inputs. Energy Convers Manage 2023;294:117596. http://dx.doi.org/10.1016/j.enconman.2023.117596.
[22] Tseronis K, Bonis I, Kookos I, Theodoropoulos C. Parametric and transient analysis of non-isothermal, planar solid oxide fuel cells. Int J Hydrog Energy 2012;37(1):530–47. http://dx.doi.org/10.1016/j.ijhydene.2011.09.062, 11th China Hydrogen Energy Conference.
[23] Srikanth S, Heddrich M, Gupta S, Friedrich K. Transient reversible solid oxide cell reactor operation – experimentally validated modeling and analysis. Appl Energy 2018;232:473–88. http://dx.doi.org/10.1016/j.apenergy.2018.09.186.
[24] Sun A, Shuai W, Zheng N, Han Y, Xiao G, Ni M, et al. Self-adaptive heat management of solid oxide electrolyzer cell under fluctuating power supply. Energy Convers Manage 2022;271:116310. http://dx.doi.org/10.1016/j.enconman.2022.116310.
[25] Tang S, Amiri A, Tadé MO. System level exergy assessment of strategies deployed for solid oxide fuel cell stack temperature regulation and thermal gradient reduction. Ind Eng Chem Res 2019;58(6):2258–67. http://dx.doi.org/10.1021/acs.iecr.8b04142.
[26] Sun Y, Zheng W, Ji S, Sun A, Shuai W, Zheng N, et al. Dynamic behavior of high-temperature CO2/H2O co-electrolysis coupled with real fluctuating renewable power. Sustain Energy Technol Assess 2022;52:102344. http://dx.doi.org/10.1016/j.seta.2022.102344.
[27] Yang Y, Tong X, Hauch A, Sun X, Yang Z, Peng S, et al. Study of solid oxide electrolysis cells operated in potentiostatic mode: Effect of operating temperature on durability. Chem Eng J 2021;417:129260. http://dx.doi.org/10.1016/j.cej.2021.129260.
[28] Chen M, Sun X, Chatzichristodoulou C, Koch S, Hendriksen PV, Mogensen MB. Thermoneutral operation of solid oxide electrolysis cells in potentiostatic mode. ECS Meeting Abstracts 2017;MA2017-03(1):287. http://dx.doi.org/10.1149/ma2017-03/1/287.
[29] Liao T, He Q, Xu Q, Dai Y, Cheng C, Ni M. Coupling properties and parametric optimization of a photovoltaic panel driven thermoelectric refrigerators system. Energy 2021;220:119798. http://dx.doi.org/10.1016/j.energy.2021.119798.
[30] macrovector. Hydrogen energy set. 2021, URL https://www.freepik.com/free-vector/hydrogen-energy-set_26762033.htm.
[31] Liang Z, Wang J, Wang Y, Ni M, Li M. Transient characteristics of a solid oxide electrolysis cell under different voltage ramps: Transport phenomena behind overshoots. Energy Convers Manage 2023;279:116759. http://dx.doi.org/10.1016/j.enconman.2023.116759.
[32] Liang Z, Wang J, Ren K, Jiao Z, Ni M, An L, et al. Discovering two general characteristic times of transient responses in solid oxide cells. Nature Commun 2024;1–12. http://dx.doi.org/10.1038/s41467-024-48785-1.
[33] Unbound Solar. 2023, URL https://unboundsolar.com/1524436/suniva/solar-panels/suniva-opt285-60-4-100-silver-mono-solar-panel.
[34] Bae Y, Lee S, Hong J. The effect of anode microstructure and fuel utilization on current relaxation and concentration polarization of solid oxide fuel cell under electrical load change. Energy Convers Manage 2019;201:112152. http://dx.doi.org/10.1016/j.enconman.2019.112152.
[35] Su Y, Zhong Z, Jiao Z. A novel multi-physics coupled heterogeneous single-cell numerical model for solid oxide fuel cell based on 3D microstructure reconstructions. Energy Environ Sci 2022;15(6):2410–24. http://dx.doi.org/10.1039/d2ee00485b.
[36] NIST. Thermophysical properties of fluid systems. 2021, URL https://webbook.nist.gov/chemistry/fluid/.
[37] Mas R, Berastain A, Antoniou A, Angeles L, Valencia S, Celis C. Genetic algorithms-based size optimization of directly and indirectly coupled photovoltaic-electrolyzer systems. Energy Convers Manage 2022;270:116213. http://dx.doi.org/10.1016/j.enconman.2022.116213.
[38] Lin M, Suter C, Diethelm S, Van herle J, Haussener S. Integrated solar-driven high-temperature electrolysis operating with concentrated irradiation. Joule 2022;6(9):2102–21. http://dx.doi.org/10.1016/j.joule.2022.07.013.
[39] Tembhurne S, Nandjou F, Haussener S. A thermally synergistic photo-electrochemical hydrogen generator operating under concentrated solar irradiation. Nat Energy 2019;4(5):399–407. http://dx.doi.org/10.1038/s41560-019-0373-7.
[40] Bard AJ, Faulkner LR, White HS. Electrochemical methods: fundamentals and applications. John Wiley & Sons; 2022.
[41] Paul B, Andrews J. Optimal coupling of PV arrays to PEM electrolysers in solar–hydrogen systems for remote area power supply. Int J Hydrog Energy 2008;33(2):490–8. http://dx.doi.org/10.1016/j.ijhydene.2007.10.040.
[42] Maroufmashat A, Sayedin F, Khavas SS. An imperialist competitive algorithm approach for multi-objective optimization of direct coupling photovoltaic-electrolyzer systems. Int J Hydrog Energy 2014;39(33):18743–57. http://dx.doi.org/10.1016/j.ijhydene.2014.08.125.
[43] Godula-Jopek A. Hydrogen production: by electrolysis. John Wiley & Sons; 2015.